

# EFFECTS OF PETROPHYSICAL, ENVIRONMENTAL, AND GEOMETRICAL PARAMETERS ON MULTI-COMPONENT INDUCTION MEASUREMENTS ACQUIRED IN HIGH-ANGLE WELLS

Robert K. Mallan and Carlos Torres-Verdín, The University of Texas at Austin

Copyright 2006, held jointly by the Society of Petrophysicists and Well Log Analysts (SPWLA) and the submitting authors.

This paper was prepared for the presentation at the SPWLA 47<sup>th</sup> Annual Logging Symposium held in Veracruz, Mexico, June 4–7, 2006.

## ABSTRACT

This paper describes a numerical study examining the effects of petrophysical, environmental, and geometrical parameters on multi-component electromagnetic (EM) induction logging measurements. Coaxial and coplanar measurements enable the estimation of resistivities parallel and perpendicular to reservoir layers. However, borehole, geometrical, environmental and petrophysical effects can significantly bias these measurements. Understanding such biasing effects will aid in the interpretation of induction measurements and subsequently provide a more accurate and reliable formation evaluation via inversion.

We perform numerical simulations of multi-component induction logging measurements with a 3D finite-difference modeling code. A suite of models is considered, including a layered reservoir with variable conditions such as borehole dip angle, invasion, and electrical anisotropy. Analysis is carried further to examine the sensitivity of the multi-component measurements to the extent of the invasion zone in a deviated well and in the presence of shoulder-bed anisotropy. Finally, we examine the response due to non-uniform invasion, generated from mud-filtrate invasion in a horizontal well.

Simulations show that shoulder-bed effects across sand layers become substantial in the presence of shoulder-bed anisotropy, even at low values of dip angle. Measurements centered about sand layers exhibit sensitivity to the depth of mud-filtrate invasion. In particular, coplanar measurements exhibit different responses for symmetric and non-symmetric invasion fronts, indicating the potential ability of multi-component tools to detect non-uniform invasion. In addition, shoulder-bed anisotropy has a considerable effect on these sensitivities, to significantly alter the assessment of invasion in terms of resistivity, depth, and front shape.

## INTRODUCTION

Presence of macroscopic electrical anisotropy, such as that resulting from thinly laminated sand-shale and

sand-sand sequences, can substantially affect conventional borehole induction measurements, thereby causing an erroneous evaluation of hydrocarbon saturation. The addition of non-symmetric and non-uniform mud-filtrate invasion resulting from highly deviated and horizontal wells presents an additional degree of complexity that is hard to differentiate from other petrophysical and environmental effects. Multi-component induction tools are now commercially available that provide additional measurements necessary to accurately characterize anisotropic near-wellbore formation properties.

Much has been reported on the use of coaxial array induction measurements in complex borehole environments (Alpak et al., 2003, Anderson et al., 1999, 1997, and Barber et al., 1995). However, relatively scant information is available discussing environmental and petrophysical effects on multi-component EM borehole measurements. Tompkins et al. (2004) analyzed borehole and invasion effects on multi-component induction measurements in a vertical well. Wang and Fang (2001) investigated multi-component responses in a deviated well, and Wang et al. (2003) examined the effects of borehole properties (mud conductivities and eccentricity) and invasion within an infinitely thick layer.

This paper examines a range of petrophysical, environmental, and geometrical parameters for their effects on multi-component induction measurements acquired in highly-deviated and horizontal wells. Special emphasis is given to the presence of electrical anisotropy in the conductive shale layers shouldering a resistive, hydrocarbon-bearing sand, and its subsequent influence on measurements across the sand layer under varying parameters, including dip angle, layer thickness, and invasion. A suite of simulations is performed for variations of the model shown in Figure 1 to examine the relative effects of borehole, shoulder-bed anisotropy, and invasion on the different components ( $H_{zz}$ ,  $H_{xx}$ , and  $H_{yy}$ ). Subsequently, we perform a systematic study of the sensitivity of multi-component induction measurements to radial lengths of invasion at various dip angles, in the presence of shoulder-bed anisotropy. In addition to parametric models, we examine models generated directly from the simulation of mud-filtrate invasion. This provides us with accurate representation of non-symmetric and non-uniform invasion as a result of well deviation, permeability anisotropy, capillary

pressure, gravity segregation, and high/low permeable layer interfaces. Our objective is to quantify the relative sensitivity of multi-component measurements to the various geometrical and petrophysical parameters in an effort to evaluate their ability to distinguish the various effects and thereby obtain an accurate and reliable characterization of formation properties.

The sensitivity analysis is performed with a finite-difference code (Hou et al., 2006) written with a coupled vector-scalar potential formulation. This code performs accurate simulations of multi-component borehole induction measurements in 3D inhomogeneous, anisotropic media over a wide range of frequencies. Extensive benchmarking of the code indicates that the accuracy of the simulations presented in this paper is no worse than 2%.

**METHODOLOGY**

Borehole EM induction logging measurements are simulated across a complex reservoir model with permeable and impermeable layers. Figure 1 shows the resistivity model considered for the numerical simulations; it consists of a sequence of reservoir layers – ranging from conductive brine-bearing to resistive hydrocarbon-bearing – shouldered by conductive shale layers. This model was adapted from an actual borehole logging situation of a dipping well in the deepwater Gulf of Mexico penetrating Tertiary unconsolidated turbidite sediments. It includes a wide range of variations of conductivity/resistivity contrasts. We simulate the measurements assuming a tool that consists of collocated multi-component magnetic receivers located 1.8, 0.7, and 0.4 m below a single collocated multi-component magnetic transmitter operating at 25, 50, and 100 kHz (Figure 2).

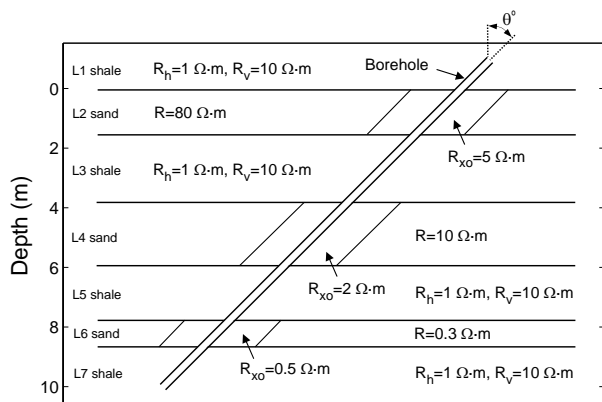


**Fig. 1:** Layered resistivity model with borehole and invasion. Diameters of the borehole and invasion are 21.59 cm and 30.48 cm, respectively. The borehole resistivity is 0.4 ohm-m, with the borehole dip angle located in the  $x$ - $z$  Cartesian plane.

The numerical simulations algorithm overlays an optimized grid onto a parameterized model domain and assigns averaged tensor conductivities to each cell. A non-uniform Cartesian grid is constructed around the tool, with a minimum grid size of 0.05 m near the transmitter and the receivers. Grid steps progressively increase outward from transmitter/receiver locations with incremental steps as described by Davydycheva et al. (2003), to the outer boundary located 1–2 skin depths away for the lowest frequency of interest. A homogeneous zero Dirichlet boundary condition is enforced at the outer grid nodes. The formation model shown in Figure 1 is superimposed onto the grid using the standard conductivity averaging approach described by Moskow et al. (1999). In the simulation examples, the simulation grid consists of  $28 \times 28 \times 92$  cells in the  $x$ ,  $y$ , and  $z$  directions, respectively. Figure 2 shows the distribution of grid nodes in the  $x$ - $z$  Cartesian plane superimposed to one of the layers included in Figure 1, dipping at an angle of  $\theta$ . The same figure shows the relative location of the transmitter and receivers. We shift the grid from one measurement point to another as the location of the tool is progressively moved along the borehole axis to reproduce a standard logging operation.

Simulated magnetic fields are denoted as  $H_{pq} = \text{Re}(H_{pq}) + i\text{Im}(H_{pq})$ , where  $\text{Re}(H_{pq})$  and  $\text{Im}(H_{pq})$  are the real (in-phase) and imaginary (quadrature) parts of the magnetic field, respectively, the first subscript  $p$  indicates the moment orientation of the magnetic transmitter, and the second subscript  $q$  indicates the orientation of the magnetic receiver. In this paper, we only examine magnetic fields pertaining to the maxi-

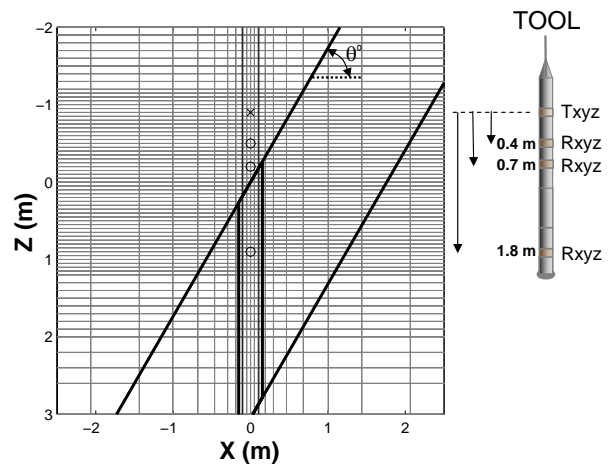


**Fig. 2:** Subset of the  $28 \times 28 \times 92$  finite-difference grid used for the numerical simulations. Overlain on the grid are the borehole and the first layer, with invasion, and dipping at  $\theta$ . To the right of the grid is a depiction of the tool configuration, roughly to scale and vertically aligned with the grid.

mum coupled components of the type  $H_{pp}$  for the simulation examples. Moreover, for the models considered, the formation response is predominantly contained in the quadrature component; therefore, the simulations presented here show only results for the quadrature component.

## NUMERICAL RESULTS

**Shoulder-bed effects** – Simulations of the model (Figure 1) with no borehole and no invasion (1D) are performed for various dip angles with the shoulder-beds being either isotropic or anisotropic. Figures 3, 4, and 5 show quadrature field responses for  $H_{zz}$ ,  $H_{xx}$ , and  $H_{yy}$ , respectively, at a frequency of 25 kHz and for a receiver offset of 1.8 m. Similarly, Figures 6, 7 and 8 show quadrature field responses for a receiver offset of 0.4 m.

Simulations indicate that the effect of shoulder-bed anisotropy on the measurements is more pronounced for the conductive (0.3 ohm-m) reservoir layer, versus a smaller, almost negligible effect, across the resistive (80 ohm-m) layer. These results reflect the model with the reservoir layers having both different resistivities and thicknesses, adding ambiguity as to which parameter, the resistivity or the thickness, influences the shoulder-bed anisotropy effect across the reservoir layer. To shed further light to this problem, we repeated the simulations, where, for each simulation, the reservoir layers were assigned the same resistivity, 80, 10, or 0.3 ohm-m. The ensuing simulations show that, for the given model, the resistivity, and not the thickness of the layer plays a significant role on the effect that shoulder-bed anisotropy has on measurements acquired across the reservoir layer.

The characteristic “horns” in the coplanar measurements are caused by the accumulation of electrical charge at bed boundaries. This charge buildup is associated with the current flowing normal to the layer boundary. With increasing dip angle, the  $H_{xx}$ -induced current flows increasingly parallel to the bed boundary and, conversely, the  $H_{zz}$ -current flow becomes increasingly normal. As a result, the horns observed in the  $H_{xx}$  response decrease with increasing dip angle. At the same time, development of horns occurs in the  $H_{zz}$  response. The horns for  $H_{yy}$  remain because the orientation of the induced current loop with respect to the layer boundary does not change with dip angle. Also, the anisotropy effect shifts  $H_{xx}$  toward positive for all of the dip angles. On the other hand,  $H_{yy}$  is shifted toward positive for the dip angles of 0° to 45° and shifted toward negative for the larger dip angles of 60° and 80°.

A subsequent suite of simulations for the main model (Figure 1) incorporates the borehole in conjunction with

invasion and shoulder-bed anisotropy — and combinations thereof. We perform these simulations over a range of dip angles. Results for a well dip angle of 80° and a frequency of 25 kHz are shown in Figures 9, 10, and 11, for a 1.8 m receiver offset and in Figures 12, 13, and 14 for a 0.4 m offset. These plots show responses for a layered model and borehole, with and without invasion, and with and without anisotropy in the shoulder-beds. The associated 1D layered simulations are included to emphasize the influence of the borehole on the shoulder-bed and invasion responses. Results indicate that the relative effect of the shoulder-bed anisotropy versus the invasion response can vary, depending on the dip angle and component configuration (ie.,  $H_{zz}$ ,  $H_{xx}$ , or  $H_{yy}$ ). In most cases, shoulder-bed anisotropy has a larger effect across the reservoir layer than invasion. In addition, the effect of the borehole can be significant, compared to the invasion response, and can also depend on the tool component, dip angle, and borehole-formation conductivity contrast.

**Invasion effects** – We examine the sensitivities of the different components ( $H_{zz}$ ,  $H_{xx}$  and  $H_{yy}$ ) to invasion in a deviated well environment. Wang et al. (2003) described invasion effects in an infinitely thick layer (whole-space) with the principal components of the electrical anisotropy aligned with the tool components, producing a diagonal conductivity tensor. Here, the shoulder-bed effects are included, and because of the

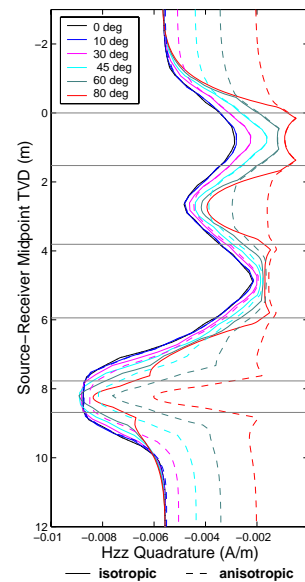


**Fig. 3:**  $H_{zz}$  quadrature field response for the model shown in Figure 1 with no borehole and no invasion (1D simulation). Receiver offset is 1.8 m, and the measurement profiles vary in dip angle  $\theta$ , measured from the normal direction to the layers. The panel shows simulations for the model with isotropic (solid lines) and anisotropic (dashed lines) shoulder-beds.

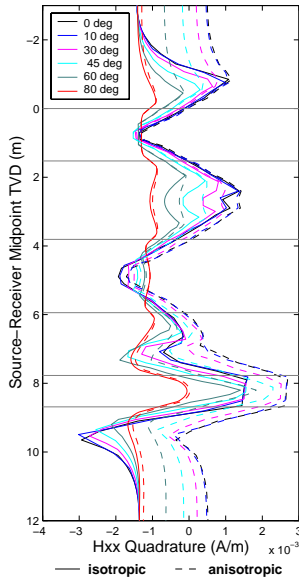


**Fig. 4:** *Hxx quadrature field response for the model shown in Figure 1 with no borehole and no invasion (1D simulation). Receiver offset is 1.8 m, and the measurement profiles vary in dip angle  $\theta$ , measured from the normal direction to the layers. The panel shows simulations for the model with isotropic (solid lines) and anisotropic (dashed lines) shoulder-beds.*

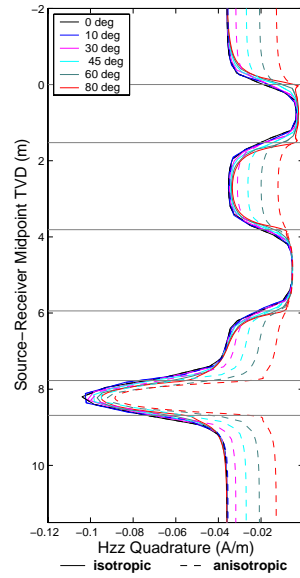


**Fig. 6:** *Hzz quadrature field response for the model shown in Figure 1 with no borehole and no invasion (1D simulation). Receiver offset is 0.4 m, and the measurement profiles vary in dip angle  $\theta$ , measured from the normal direction to the layers. The panel shows simulations for the model with isotropic (solid lines) and anisotropic (dashed lines) shoulder-beds.*

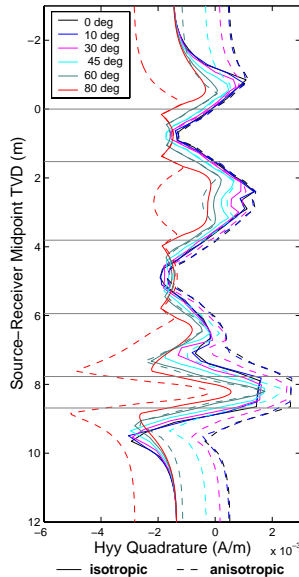


**Fig. 5:** *Hyy quadrature field response for the model shown in Figure 1 with no borehole and no invasion (1D simulation). Receiver offset is 1.8 m, and the measurement profiles vary in dip angle  $\theta$ , measured from the normal direction to the layers. The panel shows simulations for the model with isotropic (solid lines) and anisotropic (dashed lines) shoulder-beds.*

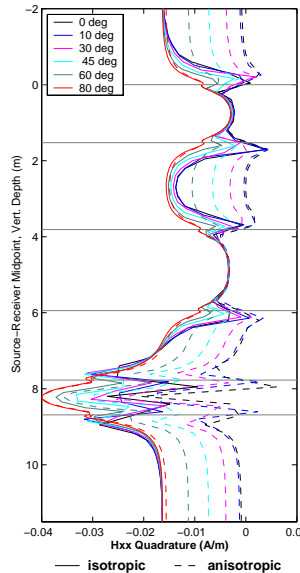


**Fig. 7:** *Hxx quadrature field response for the model shown in Figure 1 with no borehole and no invasion (1D simulation). Receiver offset is 0.4 m, and the measurement profiles vary in dip angle  $\theta$ , measured from the normal direction to the layers. The panel shows simulations for the model with isotropic (solid lines) and anisotropic (dashed lines) shoulder-beds.*

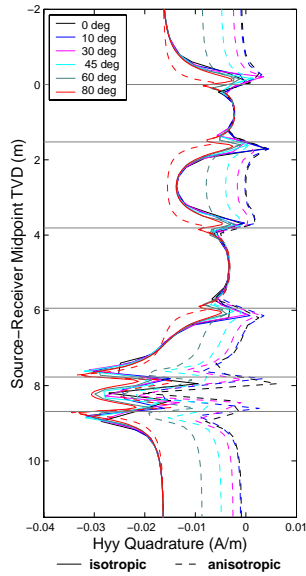


**Fig. 8:** *Hyy* quadrature field response for the model shown in Figure 1 with no borehole and no invasion (1D simulation). Receiver offset is 0.4 m, and the measurement profiles vary in dip angle  $\theta$ , measured from the normal direction to the layers. The panel shows simulations for the model with isotropic (solid lines) and anisotropic (dashed lines) shoulder-beds.

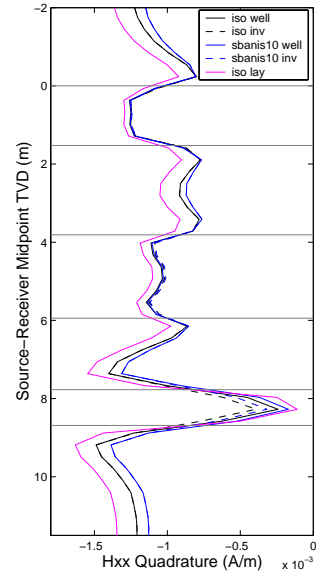


**Fig. 10:** *Hxx* quadrature field response for variants of the model shown in Figure 1. Receiver offset is 1.8 m, and the measurement profiles are at a dip angle  $\theta$  of 80°, measured from the normal direction to the layers.

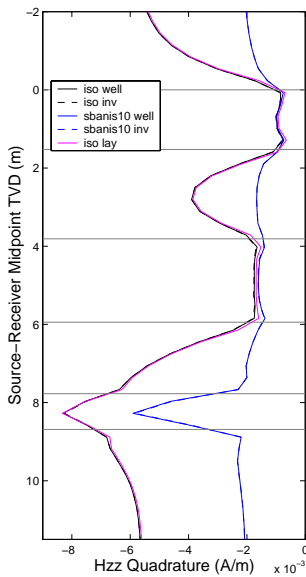


**Fig. 9:** *Hzz* quadrature field response for variants of the model shown in Figure 1. Receiver offset is 1.8 m, and the measurement profiles are at a dip angle  $\theta$  of 80°, measured from the normal direction to the layers.

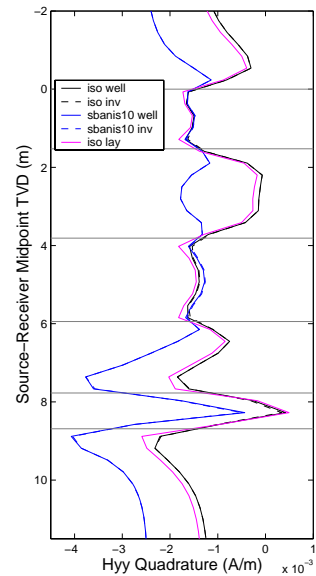


**Fig. 11:** *Hyy* quadrature field response for variants of the model shown in Figure 1. Receiver offset is 1.8 m, and the measurement profiles are at a dip angle  $\theta$  of 80°, measured from the normal direction to the layers.

deviation of the well with respect to the layers, the conductivity tensor is no longer diagonal.

To better quantify the invasion response and the subsequent effect of shoulder-bed anisotropy, we perform simulations for increasing radial lengths of invasion. The tool (1.8 m offset) source-receiver midpoint is centered in the second reservoir layer (10 ohm-m, Figure 1),

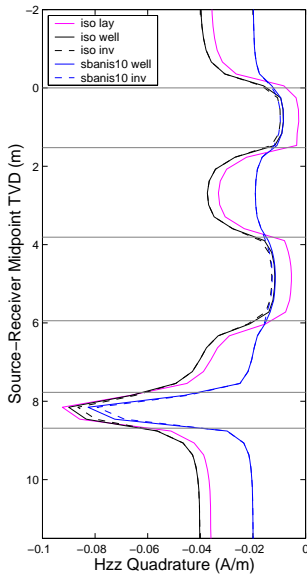


**Fig. 12:**  $H_{zz}$  quadrature field response for variants of the model shown in Figure 1. Receiver offset is 0.4 m, and the measurement profiles are at a dip angle  $\theta$  of  $80^\circ$ , measured from the normal direction to the layers.

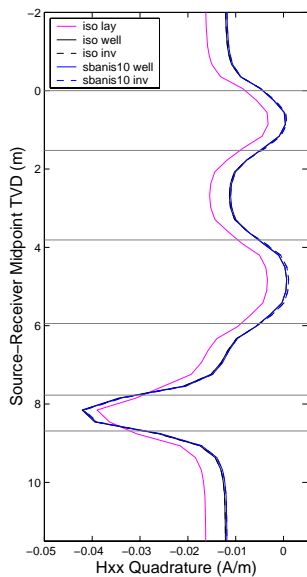


**Fig. 13:**  $H_{xx}$  quadrature field response for variants of the model shown in Figure 1. Receiver offset is 0.4 m, and the measurement profiles are at a dip angle  $\theta$  of  $80^\circ$ , measured from the normal direction to the layers.

but with the layer thickness decreased to 0.9 m to better illustrate the effect of neighboring layers. Responses are calculated for increasing values of radial length of invasion for the model with isotropic and anisotropic shoulder-beds.

Figure 15 shows  $H_{zz}$  results and Figure 16 shows  $H_{xx}$  and  $H_{yy}$  results, at a frequency of 25 kHz, for  $30^\circ$ ,  $60^\circ$ , and  $80^\circ$  dip angles. A linear shift toward positive (or decrease in response) is observed in  $H_{zz}$  at radial lengths of invasion out to a point of inflection, beyond which the deviation between the two responses increases, and the anisotropic response begins to asymptote. This distance at which the inflection in the  $H_{zz}$  component occurs decreases with increasing dip angle. The  $H_{xx}$  and  $H_{yy}$  responses can differ greatly from each other depending on the dip angle and presence of shoulder-bed anisotropy. The effect of shoulder-bed anisotropy alters the radial sensitivity in a nonlinear fashion and causes the responses to reach their asymptotic value at a shorter radial invasion length, indicating a decreased radial extent of the sensitivity. Under isotropic shoulder-bed conditions, the relative shapes of the  $H_{xx}$  and  $H_{yy}$  responses can differ significantly, depending on dip angle. However, in the presence of shoulder-bed anisotropy, the shapes of the  $H_{xx}$  and  $H_{yy}$  responses tend to parallel each other, with the exception that the inflection point occurs at a shorter distance for  $H_{yy}$ , depending on the dip angle.

Responses at a frequency of 100 kHz, shown in Figure 17, of  $H_{xx}$  and  $H_{yy}$  for  $30^\circ$ ,  $60^\circ$ , and  $80^\circ$  dip angles,

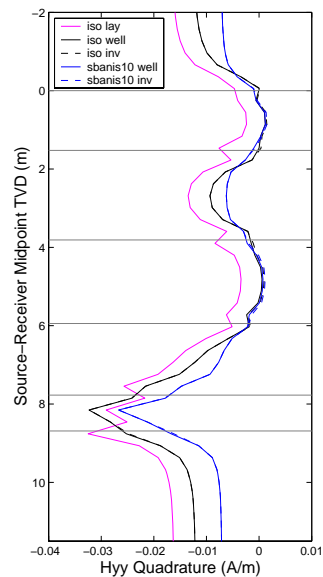


**Fig. 14:**  $H_{yy}$  quadrature field response for variants of the model shown in Figure 1. Receiver offset is 0.4 m, and the measurement profiles are at a dip angle  $\theta$  of  $80^\circ$ , measured from the normal direction to the layers.

exhibit different sensitivities to the invasion, indicating additional, unique information born by the frequency behavior of these components.

**Horizontal well** – We examine the multi-component induction response in a horizontal well environment. Alpak et al. (2003) studied the sensitivity of a coaxial array induction tool to numerically simulated mud-filtrate invasion from a horizontal well. Their simulations for the case of 25% porosity and a permeability anisotropy of  $k_h/k_v = 1, 3, 5,$  and  $10$  are considered here. We extend Alpak et al.'s (2003) model to include presence of electrical anisotropy, borehole eccentricity, and a resistive, oil-based mud.

A 2D distribution of electrical conductivity is calculated from water saturation and salt concentration distributions described by Alpak et al. (2003), using Archie's equation (Archie, 1942),

$$\sigma = (1/a)\sigma_w\phi^m S_w^n, \quad (1)$$

where  $\sigma$ ,  $\sigma_w$ ,  $\phi$ , and  $S_w$  denote the formation conductivity, brine conductivity, porosity, and brine saturation, respectively, and the terms  $a$ ,  $m$ , and  $n$  are empirical constants. The brine conductivity is calculated with the equation (Zhang et al., 1999)

$$\sigma_w = \left[ \left( 0.0123 + \frac{3647.5}{C_w^{0.955}} \right) \frac{82}{1.8T + 39} \right]^{-1}, \quad (2)$$

where  $C_w$  is the simulated salt water concentration and  $T$  is the formation temperature in [ $^{\circ}\text{C}$ ]. Figure 18 shows a subset of the calculated conductivity distributions for the different cases of permeability anisotropy. This scalar conductivity grid is mapped, using bilinear interpolation, to a  $44 \times 44$   $xy$ -grid with an outer boundary similar to that used in the previous EM logging simulations. The  $xy$ -planar conductivities are copied in the  $z$ -direction of the grid, generating a 3D mesh to accommodate the 3D EM finite-difference modeling code.

Multi-component induction responses are calculated for multiple receiver offsets, ranging from 0.4 m to 1.8 m, at a frequency of 100 kHz. These responses are converted to apparent conductivity via

$$\sigma_{app} = K_{pp} \cdot \text{Imag}(H_{pp}), \quad (3)$$

where  $K$  is a calibration constant relating the analytical whole-space response of a magnetic dipole to a whole-space conductivity of 0.28 (S/m), which is the background formation conductivity associated with simulations of mud-filtrate invasion.

Figure 19 shows  $H_{zz}$ ,  $H_{xx}$ , and  $H_{yy}$  responses for the models shown in Figure 18. Field responses are included for a whole-space, to reference the true formation conductivity, and for a well with no invasion to reference the borehole effect. For all models, invasion responses are distinguishable from those with no invasion. With

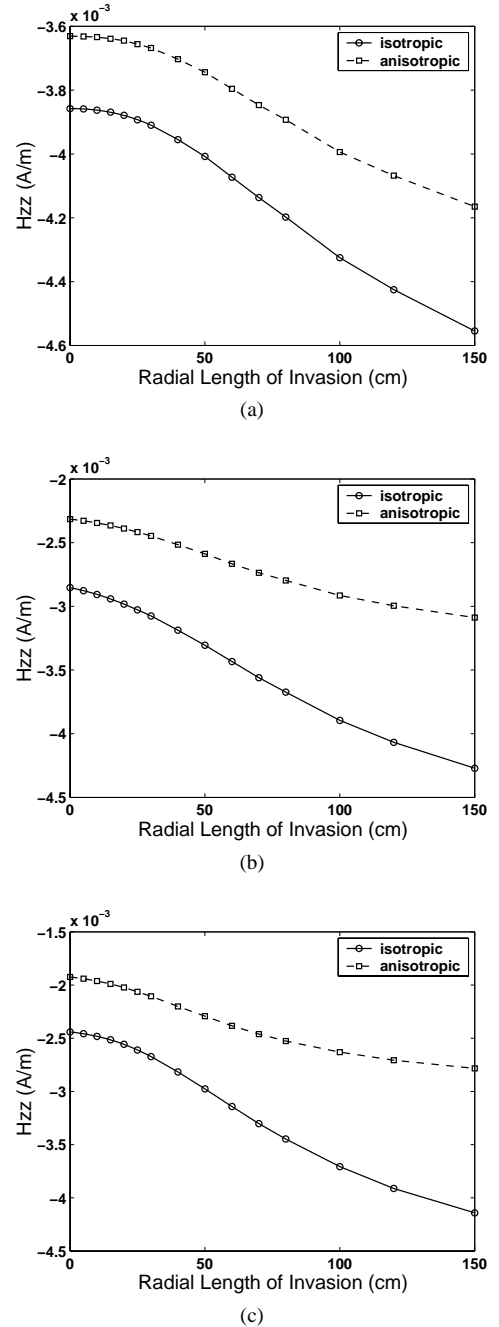


**Fig. 15:**  $H_{zz}$  quadrature field response versus radial length of invasion for the 3D model shown in Figure 1, with and without electrical anisotropy in the shale layers. Receiver offset is 1.8 m and the tool is centered in the 10 ohm-m layer having a thickness of 0.9 m. The well dip angle is (a)  $30^\circ$ , (b)  $60^\circ$ , and (c)  $80^\circ$ .

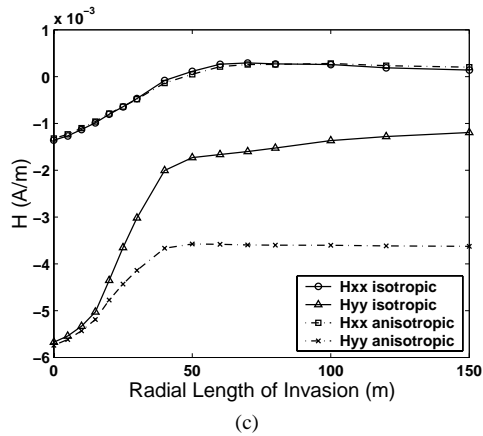
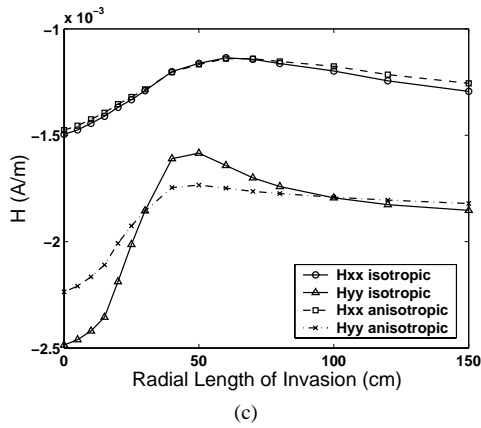
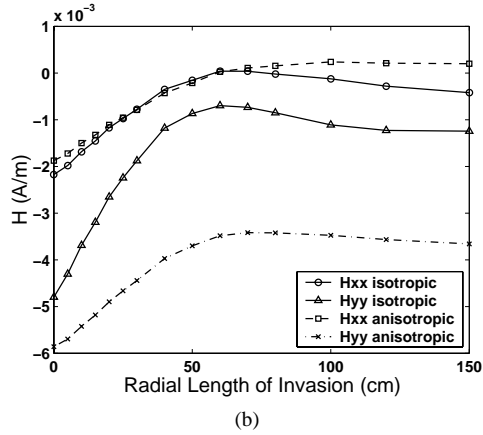
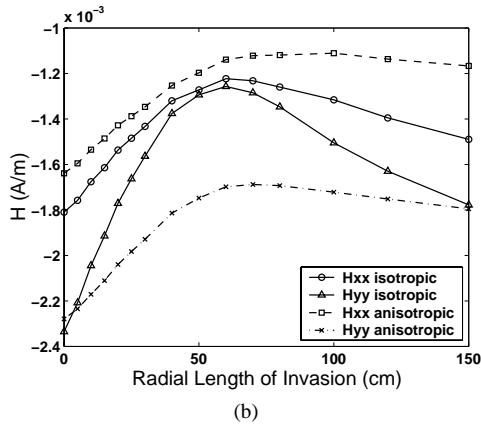
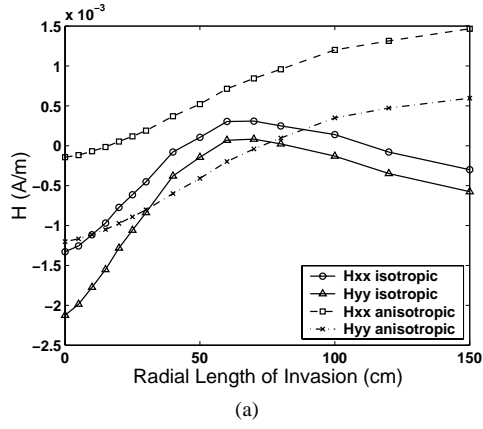
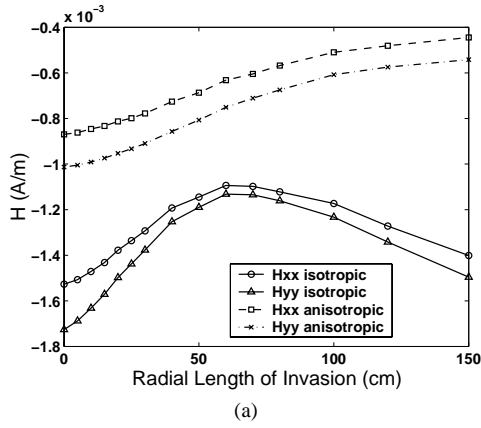


**Fig. 16:** *Hxx* and *Hyy* quadrature field response versus radial length of invasion for the 3D model shown in Figure 1, with and without electrical anisotropy in the shale layers. Receiver offset is 1.8 m and the tool is centered in the 10 ohm-m layer having a thickness of 0.9 m. The well dip angle is (a) 30°, (b) 60°, and (c) 80°.

**Fig. 17:** *Hxx* and *Hyy* quadrature field response versus radial length of invasion for the 3D model shown in Figure 1, with and without electrical anisotropy in the shale layers. Receiver offset is 1.8 m and the tool is centered in the 10 ohm-m layer having a thickness of 0.9 m. The well dip angle is (a) 30°, (b) 60°, and (c) 80°. The transmitter frequency is 100 kHz

exception of the  $k_h/k_v = 1$  case, the  $H_{zz}$  and  $H_{yy}$  invasion responses differ negligibly among the cases. The  $H_{xx}$  responses, however, are distinguishable from the different models.

The analysis is extended for the  $k_h/k_v = 10$  case to include the effect of electrical anisotropy, borehole eccentricity, and resistive, oil-based mud. Anisotropic conductivities are assigned to individual cells, where the vertical conductivity,  $\sigma_{yy}$ , is reduced with respect to the horizontal conductivities,  $\sigma_{xx}$  and  $\sigma_{zz}$  (which represent the interpolated scalar conductivity). Borehole eccentricity is simulated by shifting the tool, or the  $xy$ -grid center, downward in the  $y$ -direction by 5 cm — approximately half-way to the borehole wall.

Figure 20 shows results for these simulation cases that include electrical anisotropy and borehole eccentricity. The effect of anisotropy uniformly shifts the  $H_{zz}$  and  $H_{yy}$  responses to a decreased and increased apparent conductivity, respectively. By contrast, the  $H_{xx}$  response change is nonlinear, with the apparent conductivity increasing with increasing receiver offset. In all components, the eccentricity uniformly shifts the responses, with a more pronounced shift occurring in the  $H_{xx}$  component, causing a decrease in apparent conductivity for  $H_{zz}$  and an increase for  $H_{xx}$  and  $H_{yy}$ .

Anisotropy and eccentricity effects are repeated for the borehole conductivity decreased to 0.001 (S/m) to simulate presence of oil-based mud. Although the conductivity distributions outside the borehole (in Figure 18) do not represent the invasion of an oil-based mud, we nevertheless wish to examine the difference in response between conductive and resistive boreholes (muds) for a given formation conductivity distribution.

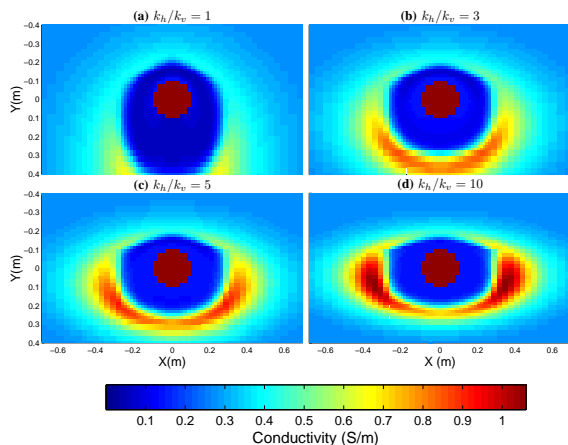


**Fig. 18:** Conductivity distributions calculated from horizontal mud-filtrate simulations described by Alpak *et al.* (2003). Panels (a), (b), (c), and (d) show cases for permeability anisotropy with  $k_h/k_v = 1, 3, 5,$  and  $10,$  respectively.

The relative effect of anisotropy on the  $H_{zz}$  and  $H_{xx}$  responses is similar to that for the conductive mud, in that  $H_{zz}$  is uniformly shifted and  $H_{xx}$  increases with receiver offset. By contrast, the  $H_{yy}$  change is no longer parallel, but decreases with increasing receiver offset. The eccentricity effect is a smaller shift, compared to the conductive mud case, with the shift in  $H_{xx}$  being negligible, and the shift in  $H_{yy}$  being in the opposite direction (a decrease in conductivity).

## DISCUSSION

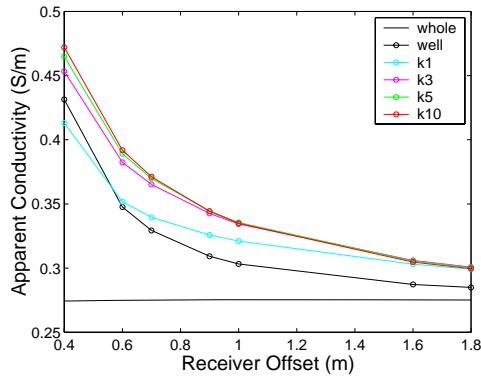
This study is a preamble to inversion. It is difficult to intuitively comprehend the intricate information included in multi-component induction measurements, however, an understanding of the nature and sensitivities of these measurements to various petrophysical, environmental, and geometrical effects may be incorporated into inversion algorithms. For instance, subsets of the measurements having greater sensitivity to specific effects/features may be used in a data adaptive inversion scheme. Furthermore, a rudimentary assessment of the formation properties, such as layer orientation, may be interpreted from the raw measurements and used in a starting model (initial guess) of an iterative inversion process.

## CONCLUSIONS

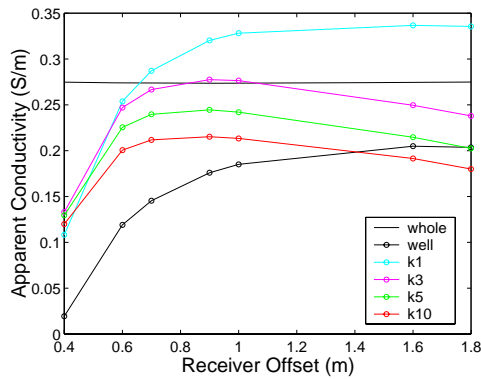
Shoulder-bed anisotropy has a measurable effect on induction logging responses across a sand layer. Both borehole dip angle and conductivity of the sand layer determine the relative contribution of this effect on the measurements, causing possible non-uniqueness in distinguishing true formation properties.

For the radial length of invasion considered in the model (Figure 1), the shoulder-bed anisotropy effect is, in most of the cases presented, much more pronounced than the invasion response. Consequently, it is important to accurately account for shoulder-bed anisotropy to correctly estimate the invasion characteristics.

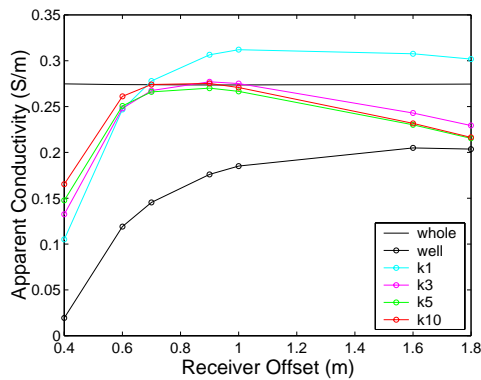
The sensitivity of the induction tool to radial length of invasion is also affected by shoulder-bed anisotropy. For isotropic shoulder beds, the various EM measurement components exhibit distinguishable sensitivities with respect to each other, indicating their ability to determine the shape of the invasion front. We note, however, that the shapes of these responses can be very sensitive to dip angle. Consequently, an accurate measure of the dip angle between the borehole and the layer is vital to correctly assess presence and shape of invasion. However, shoulder-bed anisotropy causes the sensitivity responses to reach their asymptotic value at a shorter invasion length, thereby indicating a decrease in the radial length of sensitivity. Furthermore, the relative



(a)  $\sigma_{zz}$

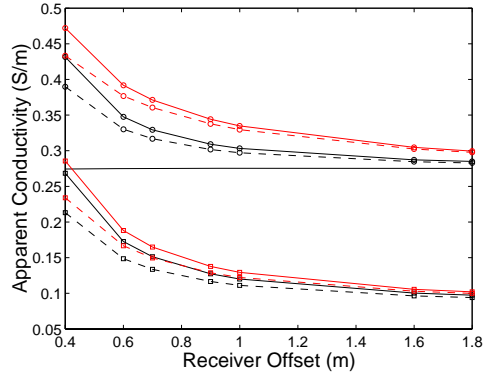


(b)  $\sigma_{xx}$

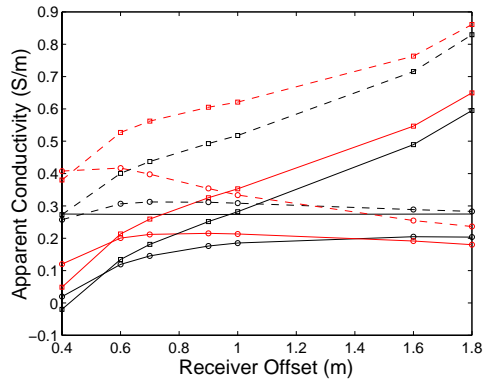


(c)  $\sigma_{yy}$

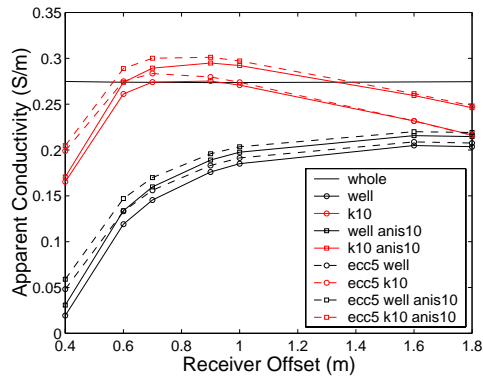
**Fig. 19:** Simulations of apparent conductivity versus receiver offset for the conductivity distributions in Figure 18. The panels show (a)  $\sigma_{zz}$  obtained from  $H_{zz}$ , (b)  $\sigma_{xx}$  obtained from  $H_{xx}$ , and (c)  $\sigma_{yy}$  obtained from  $H_{yy}$ . Also included are results for a background whole-space and for the well with no invasion. The tool frequency is 25 kHz.



(a)  $\sigma_{zz}$



(b)  $\sigma_{xx}$



(c)  $\sigma_{yy}$

**Fig. 20:** Simulations of apparent conductivity versus receiver offset for the conductivity distribution in Figure 18d ( $k_h/k_v = 10$ ). The panels show (a)  $\sigma_{zz}$  obtained from  $H_{zz}$ , (b)  $\sigma_{xx}$  obtained from  $H_{xx}$ , and (c)  $\sigma_{yy}$  obtained from  $H_{yy}$ . The panels include simulations for cases with electrical anisotropy and well eccentricity. For each case, the response for a borehole and no invasion is included for reference. Also included is the result for a background whole-space. The tool frequency is 25 kHz.

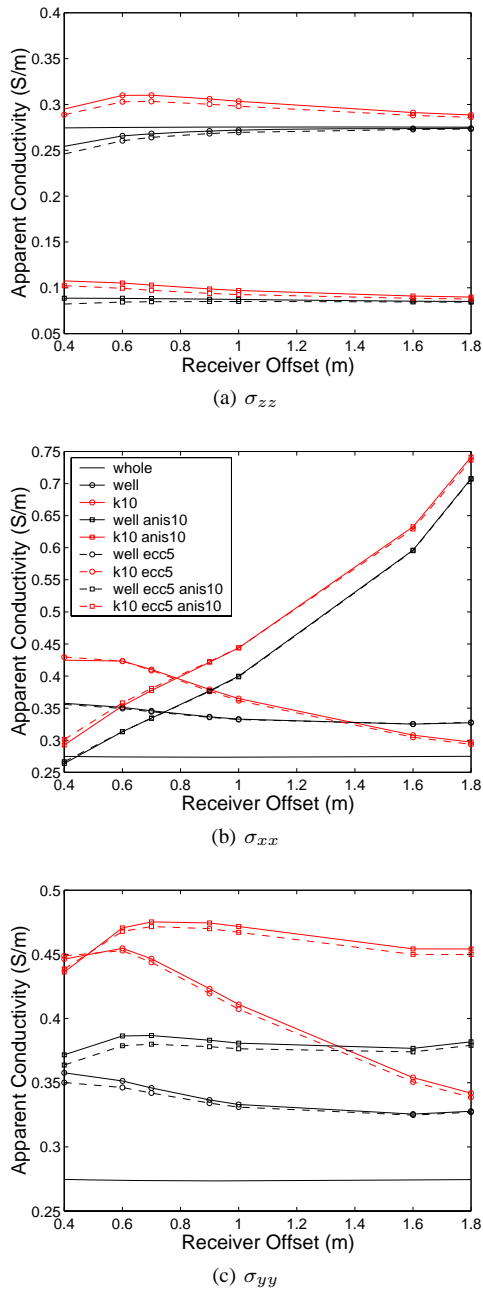


**Fig. 21:** Simulations of apparent conductivity versus receiver offset for the conductivity distribution in Figure 18d ( $k_h/k_v = 10$ ), but with the borehole conductivity decreased to 0.001 (S/m) to represent an oil-based mud. The panels show (a)  $\sigma_{zz}$  obtained from  $H_{zz}$ , (b)  $\sigma_{xx}$  obtained from  $H_{xx}$ , and (c)  $\sigma_{yy}$  obtained from  $H_{yy}$ . The panels include simulations for cases with electrical anisotropy and well eccentricity. For each case, the response for a borehole and no invasion is included for reference. Also included is the result for a background whole-space. The tool frequency is 25 kHz.

shapes of the  $H_{xx}$  and  $H_{yy}$  responses become similar, suggesting that the ability to estimate the invasion front from these components is impaired.

Simulations for the case of a horizontal well indicate that mud-filtrate invasion entails unique responses in the  $H_{xx}$  component, demonstrating the sensitivity of multi-component induction measurements to the shape and spatial extent of the invasion front. Presence of electrical anisotropy causes a uniform shift in the apparent conductivities estimated from  $H_{zz}$  and  $H_{yy}$ . By contrast, the conductivity estimated from  $H_{xx}$  has a distinguishable nature, in that it increases with increasing receiver offset. This feature could be used to quantify presence of electrical anisotropy in a horizontal well environment.

## ACKNOWLEDGMENTS

Funding for the work reported in this paper was provided by UT Austin's Research Consortium on Formation Evaluation, jointly sponsored by Aramco, Baker Atlas, BP, British Gas, ConocoPhillips, Chevron, ENI E&P, ExxonMobil, Halliburton Energy Services, Marathon, Mexican Institute for Petroleum, Norsk-Hydro, Occidental Petroleum Corporation, Petrobras, Schlumberger, Shell International E&P, Statoil, Total, and Weatherford.

## REFERENCES

- Anderson, B., Barber, T., Druskin, V., Lee, P., Dussan V., E., Knizhnerman, L., and Davydycheva, S., 1999, The response of multiarray induction tools in highly dipping formations with invasion and in arbitrary 3D geometries, *The Log Analyst*, v. 40, n. 5, p. 327–344.
- Anderson, B., Druskin, V., Habashy, T., Lee, P., Lüling, M., Barber, T., Grove, G., Lovell, J., Rosthal, R., Tabanou, J., Kennedy, D., and Shen, L., 1997, New dimensions in modeling resistivity: *Oilfield Review*, v. 9, p. 40–56.
- Alpak, O., Dussan V., E., Habashy, T., and Torres-Verdín, C., 2003, Numerical simulation of mud-filtrate invasion in horizontal wells and sensitivity analysis of array induction tools: *Petrophysics*, v. 44, n. 6, p. 396–411.
- Archie, G. E., 1942, The electrical resistivity log as an aid in determining some reservoir characteristics, *Petroleum Transactions of the AIME*, vol. 146, p. 54–62.
- Davydycheva, S., V. Druskin, and T. Habashy, 2003, An efficient finite-difference scheme for electromagnetic logging in 3D anisotropic inhomogeneous media: *Geophysics*, 68, 1525–1536.

Hou, J., Mallan, R. K., and Torres-Verdín, C., 2006, Finite-difference simulation of borehole EM measurements in 3D anisotropic media using coupled scalar-vector potentials: *Geophysics*, *in press*.

Moskow, S., V. Druskin, T. Habashy, P. Lee, and S. Davdycheva, 1999, A finite difference scheme for elliptic equations with rough coefficients using a Cartesian grid nonconforming to interfaces: *SIAM Journal on Numerical Analysis*, 36, 442-464.

Tompkins, M.J., Alumbaugh, D.L., Stanley, D.T., and Lu, X., 2004, Numerical analysis of near-borehole and anisotropic layer effects on the response of multicomponent induction logging tools: *Geophysics*, v. 69, n. 1, p. 140–151.

Wang, T. and Fang, S., 2001, 3-D electromagnetic anisotropy modeling using finite differences: *Geophysics*, v. 66, n. 5, p. 1386–1398.

Wang, T., Yu, L., and Fanini, O., 2003, Multicomponent induction response in a borehole environment: *Geophysics*, v. 68, n. 5, p. 1510–1518.

Zhang, J-H., Hu, Q., and Liu, Z-H., 1999, Estimation of true formation resistivity and water saturation with a time-lapse induction logging method: *The Log Analyst*, vol. 40, no. 2, p. 138–148.

Board of the Journal of Electromagnetic Waves and Applications, and is associate editor for *Petrophysics* (SPWLA) and the *SPE Journal*.

Email: cverdin@mail.utexas.edu

## ABOUT THE AUTHORS

**Robert K. Mallan** received a BS in Physics from East Central University in Oklahoma in 1990, and a MS in Geophysical Engineering at the University of Arizona, Tucson, in 1995. During 1996-2003, he worked for ElectroMagnetic Instruments (Richmond, CA) on the development and application of borehole EM induction logging and magnetotelluric technologies. He is currently pursuing a PhD at the Department of Petroleum and Geosystems Engineering of The University of Texas at Austin. His research is focused on petrophysics based modeling and inversion of electromagnetic well logging data in dipping and anisotropic formations.

Email: rkmallan@mail.utexas.edu

**Carlos Torres-Verdín** received a Ph.D. in Engineering Geoscience from the University of California, Berkeley, in 1991. During 1991-1997, he held the position of Research Scientist with Schlumberger-Doll Research. From 1997-1999, he was Reservoir Specialist and Technology Champion with YPF (Buenos Aires, Argentina). Since 1999, he has been with the Department of Petroleum and Geosystems Engineering of The University of Texas at Austin, where he holds the position of Associate Professor and conducts research in formation evaluation, well logging, and integrated reservoir characterization. He has served as Guest Editor for *Radio Science*, and is currently a member of the Editorial